ROYAL SOCIETY OF CHEMISTRY

PAPER

A conductive ZnO–ZnGaON nanowire-array-on-a-film photoanode for stable and efficient sunlight water splitting†

Miao Zhong,[a] Yanhang Ma,[b] Peter Oleynikov,[b] Kazunari Domen[a] and Jean-Jacques Delaunay*[a]

We report highly stable and efficient sunlight water splitting on a ZnO–ZnGaON nanowire-array-on-a-film photoanode without the assistance of any co-catalyst. The single crystalline ZnO–ZnGaON nanowire-array-on-a-film photoanode was synthesized *via* a high-temperature vapor-phase diffusion reaction of gallium (Ga) and nitrogen (N) on a single crystal domain ZnO nanowire-array-on-a-film structure. The synthesized ZnO–ZnGaON photoanode offers visible light absorption through N incorporation, improved electrical conductivity *via* Ga incorporation, and structural advantages with the high-aspect-ratio nanowire array. Compared to the chemically unstable ZnO nanowire photoanode, the ZnO–ZnGaON nanowire photoanode significantly improves the anti-photocorrosive ability for water splitting. A highly stable photocurrent density of ∼1.5 mA cm^{-2} is obtained with the ZnO–ZnGaON nanowire photoanode at an applied bias of 0.8 V_{RHE} under continuous sunlight illumination over five hours without noticeable degradation.

Photoelectrochemical (PEC) water splitting is regarded as a promising solution to produce H$_2$, a renewable energy carrier, from abundant and clean resources of sunlight and water.[1–6] In principle, sunlight photons are captured to generate electrons and holes in semiconductor photoelectrodes and the photo-generated electrons and holes that have sufficient energy drive the red-ox chemical reactions to decompose water into H$_2$ and O$_2$. A fundamental issue of the PEC technique is development of high-efficiency and long-lived PEC water splitting systems.[7–12] The PEC efficiency has been limited in the energy transfer process, involving light absorption, photogenerated electron–hole separation and water red-ox chemical reactions. Photo-electrode–photovoltaic tandem design enables broad-spectrum light absorption and, thus, realizes high PEC efficiencies.[13–15] Surface decoration of photoelectrodes with robust electrolytic co-catalysts can also enhance the water splitting efficiency owing to the improved water red-ox reaction kinetics.[16–19] Although these advances significantly improve the PEC water splitting performances, further efforts should be dedicated to reduce the fabrication cost for the complex photoelectrode–photovoltaic tandem structures and suppress the deactivation of co-catalysts in a water corrosive environment. As an essential part in a tandem or a single-junction PEC water splitting cell, the photoelectrode itself functioning efficiently and stable without the assistance of any co-catalyst is of great importance. This relies on the development of high performance photo-anode materials.

ZnO:GaN is an attractive photocatalytic material for sunlight water splitting,[20] because it possesses several important properties of visible light absorption, appropriate band edge positions enabling overall water splitting with a small onset potential, and strong resistance to photocorrosion. Sustained effort in synthesizing and improving ZnO:GaN powder materials has resulted in the demonstration of long lifetime photocatalytic water splitting under visible light illumination over three months with the assistance of Rh$_{2-y}$Cr$_y$O$_3$ co-catalysts.[21] However, it is still challenging to achieve high-efficiency water splitting with the reported ZnO:GaN powder. This is likely due to an unwanted recombination between the photogenerated electrons and holes in ZnO:GaN powder. To address the charge recombination shortfall, synthesis of high quality ZnO:GaN nanostructures to suppress the electron diffusion toward the ZnO:GaN/electrolyte interface is a possible approach. Moreover, assembly of the ZnO:GaN nanostructures into a conductive electrode enables the use of an external electric field to further enhance the charge separation at the ZnO:GaN/electrolyte interface for improved PEC performance. In this study, we demonstrate a conductive ZnO–ZnGaON nanowire-array-on-a-film photoanode realizing efficient water splitting without using

[a]*School of Engineering, The University of Tokyo, 7-3-1 Hongo, Bunkyo-Ku, Tokyo 113-8656, Japan. E-mail: jean@mech.t.u-tokyo.ac.jp; Fax: +81-3-5841-0441; Tel: +81-3-5841-3017*

[b]*Department of Materials and Environmental Chemistry, Stockholm University, SE-10691 Stockholm, Sweden*

† Electronic supplementary information (ESI) available. See DOI: 10.1039/c3ee43806f

This journal is © The Royal Society of Chemistry 2014

*Energy Environ. Sci.*, 2014, 7, 1693–1699 | **1693**

any co-catalyst. Compared to the ZnO nanowire photoanode, the synthesized ZnO–ZnGaON photoanode significantly enhances the chemical stability in electrolyte and can efficiently generate O_2 under sunlight illumination over five hours when used in a PEC water splitting cell.

The ZnO–ZnGaON nanowire-array-on-a-film structure was fabricated by a high-temperature vapor-phase diffusion reaction of Ga and N into a pre-synthesized single crystal domain ZnO nanowire-array-on-a-film sample. In principle, the diffusion reaction of Ga and N into ZnO crystals can be used to obtain high crystalline quality ZnGaON materials, because (1) Ga and N have close atomic sizes to those of Zn and O, respectively, and (2) both GaN and ZnO have the same wurtzite structure with similar lattice parameters. In our process, a careful control of the synthesis conditions is required to obtain a conductive and visible-light-sensitive single crystalline ZnO–ZnGaON nanowire-array-on-a-film structure over a large area. The ZnO nanowire-array-on-a-film structure serves as a backbone realizing a path for electrical charge transport, thus achieving good conductivity. The ZnGaON surface acts as an anti-photocorrosive and visible-light-sensitive surface for stable sunlight water oxidation. The nanowire array structure largely increases the photoanode/electrolyte interface area for the promotion of water oxidation reaction. Finally, the ZnO and ZnGaON have suitable energy band positions[22] to thermodynamically increase the migration of photogenerated holes toward the nanowire/electrolyte interface for water oxidation reaction (see Scheme 1).

Different from the reported synthesis techniques for the ZnGaON powders[20–22] and nanoparticles[23,24] obtained via direct annealing of ZnO powder and Ga_2O_3 powder in an ammonia environment, a two-step CVD process was used in this study to synthesize the large-scale single crystalline ZnO–ZnGaON nanowire-array-on-a-film structure. A single crystal domain textured ZnO nanowire-array-on-a-film sample (evidenced by XRD rocking curve and XRD pole figure analyses) was first

synthesized through a thermal CVD process using ~2 nm pre-coated Au as a CVD growth catalyst. The details are discussed in our previous report.[25] The synthesized ZnO nanowire-array-on-a-film sample was then used as a template substrate in subsequent CVD processes to synthesize the ZnO–ZnGaON nanowire-array-on-a-film sample. The ZnO template substrate was placed at a temperature of 800 °C in the CVD furnace tube and a powder mixture of Ga_2O_3 and graphite (0.12 g with a Ga_2O_3–graphite mass ratio of 5 : 1) was placed at a temperature of 1150 °C to form Ga vapor upstream the ZnO template substrate. Argon and oxygen (10 : 1 in volume ratio) were flowed through the furnace at a working pressure of 50 mbar. After a 5 minute CVD process, the deposition of Ga into ZnO was done and then the sample was annealed for another 20 minutes under an ammonia environment at a pressure of 30 mbar to obtain the ZnO–ZnGaON nanowire-array-on-a-film sample. A parametric study was performed to understand the effect of growth temperature in the second CVD process for the formation of ZnO–ZnGaON nanowire samples with different optoelectronic qualities, as discussed in detail in the ESI (see Fig. S1†).

The scanning electron microscopy (SEM) images of the ZnO and ZnO–ZnGaON nanowire-array-on-a-film samples reveal clear difference in morphology (Fig. 1). The tilted-angle SEM images show that highly uniform and densely assembled ZnO (Fig. 1a) and ZnO–ZnGaON (Fig. 1b) nanowire arrays grew over large areas. It appears that the nanowire-array-on-a-film
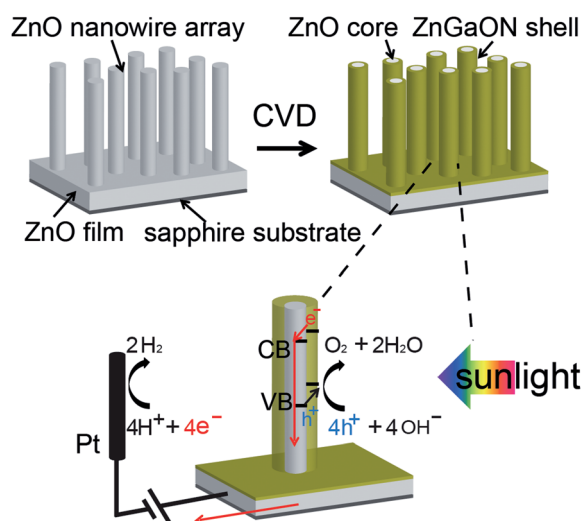
Scheme 1 Schematic of the ZnO–ZnGaON nanowire-array-on-a-film structure and the photogenerated electron–hole transfer process (ref. 22).
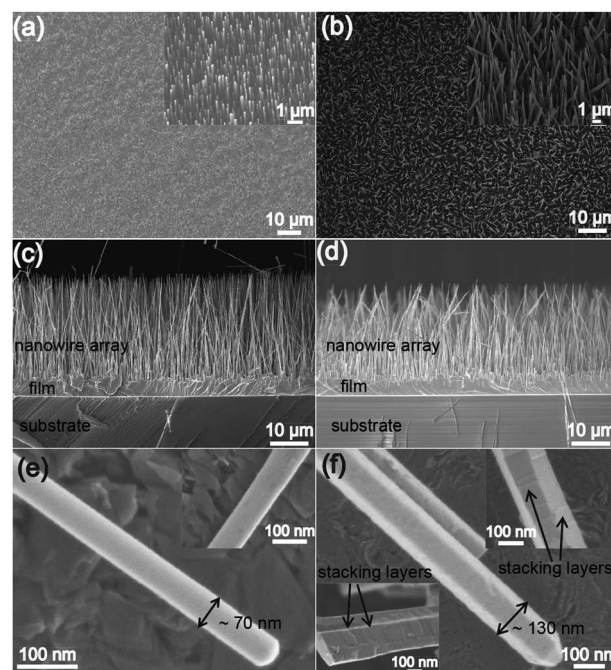
Fig. 1 The morphology of the ZnO and ZnO–ZnGaON nanowire-array-on-a-film structures: (a and b) tilted-angle SEM images of dense nanowire arrays over large areas; insets in (a) and (b) are close-up views of the vertically aligned ZnO nanowires and ZnO–ZnGaON nanowires; (c and d) cross-sectional SEM images of the ZnO and ZnO–ZnGaON long nanowires standing on thick films. (e and f) High resolution SEM images of the single ZnO and ZnO–ZnGaON nanowires.

1694 | *Energy Environ. Sci.*, 2014, **7**, 1693–1699

This journal is © The Royal Society of Chemistry 2014

structure is maintained after the CVD processes, indicating reliable syntheses of the nanowire-array-on-a-film samples. The average diameters of the ZnO and ZnO–ZnGaON nanowires are estimated to be ~70–100 nm and ~120–150 nm, respectively. Furthermore, the ZnO and ZnO–ZnGaON nanowire arrays are directly rooted in thick films (about 4.5 μm in thickness) as revealed in the cross-sectional SEM images of Fig. 1c and d. The thick film made of the same materials underneath the nanowires provides a path for the electrons to circulate and, thus, favor the formation of a conductive nanowire array-on-a-film structure. The length of the ZnO and ZnO–ZnGaON nanowires is about 25 μm. Such long nanowires significantly increase the surface areas of the samples by a factor larger than 100 compared to its smooth film counterpart, realizing a large nanowire/electrolyte contact area for PEC water splitting. The fine surface details of the ZnO and ZnO–ZnGaON nanowires are clearly observed in high resolution SEM (HRSEM) images taken with a JEOL JSM-7401F (resolution of 1.5 nm at 1 kV) using back scattered electrons at a 3.0 mm working distance. As shown in Fig. 1e and f, HRSEM images reveal an increase in diameter of nanowires from ~70 to ~130 nm after incorporation of Ga and N. Besides, ZnO and ZnGaON nanowires present different surface features under the same observation conditions, namely, smoothness for ZnO but roughness for ZnGaON. Discontinuous layers or fragments were observed on the surface of ZnGaON nanowires, indicating a vapor–solid growth of the ZnGaON layers in our second CVD process.

Substantial differences in the constituent compositions and chemical states in the ZnO and ZnO–ZnGaON nanowire samples are evidenced by XPS analyses. Fig. 2a compares the XPS wide-scan survey spectra of the ZnO and ZnO–ZnGaON samples. In the XPS survey spectrum of the ZnO sample, binding energy peaks of the Zn and O elements are detected.[26]

In contrast, binding energy peaks of the Zn, O, Ga and N elements are detected in the XPS survey spectrum of the ZnO–ZnGaON sample. This is clear evidence for the formation of ZnGaON compounds on the surface of the ZnO nanowires upon the vapor-phase Ga and N diffusion reaction process. To further clarify the elemental distributions in the ZnO–ZnGaON nanowire sample, an XPS depth profile analysis was carried out using non-reactive Ar ion etching at an estimated sputtering rate of ~2 nm per minute. As shown in Fig. 2b, the Zn, Ga, O and N elements are continuously detected in this XPS depth profile analysis (each Ar etching lasts for 30 seconds). The intensity of the N 1s peak shows no obvious difference upon Ar ion etching, indicating N incorporation into the nanowires. In addition, the depth profile of the Zn/Ga atomic ratio was estimated from the intensities of Zn and Ga peaks. As shown in Fig. 2d, a significant increase in the Zn/Ga atomic ratio from ~0.6 to 1 is obtained with the etching depth, indicating that more Zn is present inside the nanowires. This result is in agreement with the method of diffusion reaction of Ga into ZnO in our CVD process.

The formation of ZnGaON on the surface of the ZnO nanowires has been confirmed. We further identify the chemical states of each element in the ZnGaON compounds. As reported in the literature,[27] Ga is easily incorporated into ZnO to form Ga doped ZnO or $ZnGa_2O_4$ through high temperature CVD processes. The peak positions of Zn 2p, Ga 2p and O 1s in the XPS spectrum of the ZnO–ZnGaON sample indicate Zn^{2+}, Ga^{3+}, and O^{2-} chemical states, thus confirming that Ga is chemically incorporated into ZnO. In the case of N, it is always challenging to incorporate N into ZnO at a sufficient amount for the ZnO band gap to be narrowed without degrading its electrical conductivity. This problem is avoided in our ZnO–ZnGaON sample because Ga is co-incorporated with N into the ZnO nanostructures in a carefully controlled CVD process. The estimated percentage of N is roughly ~25% in the measured surface layers of the ZnO–ZnGaON sample by calculating the intensities of the Zn, Ga, O, N peaks in the XPS spectrum. Moreover, the high resolution XPS spectrum of the N 1s peak shown in Fig. 2c reveals that the binding energy of N 1s is between 396 and 397 eV. This binding energy value is in agreement with the N^{3-} chemical state in metal nitrides such as Ga–N (~396.5 eV) or Zn–N (~396.2 eV),[28–31] in which N atoms receive substantial charge from the surrounding metal atoms. Note that N chemical bonds in N–H amines (binding energy of ~399.6 eV), NO_2 nitrite (~404.5 eV), N_2 diatomic nitrogen (~404.9 eV) and NO_3 nitrate (~406.8 eV), which always render the optoelectronic quality of the ZnGaON material difficult to control, are not detected in our sample. Therefore, the XPS results indicate that Ga and N are chemically incorporated into ZnO to form the ZnGaON compound.

To understand the crystalline quality of the ZnO and ZnO–ZnGaON nanowire samples, standard X-ray diffraction (XRD) $\theta/2\theta$ analyses were performed. In our case, the XRD technique is favorable to be used for the characterization of the ZnO and ZnO–ZnGaON samples, because (1) XRD results represent the crystalline quality of the ZnO and ZnO–ZnGaON electrodes over a centimeter scale, (2) compared to electron diffraction
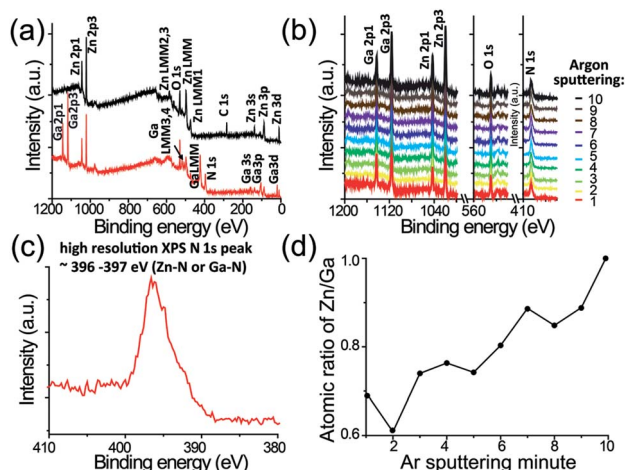

Fig. 2 XPS analyses of the ZnO and ZnO–ZnGaON nanowire-array-on-a-film samples: (a) wide-scan XPS survey spectra of the ZnO and ZnO–ZnGaON samples; (b) XPS depth profile spectra of the ZnO–ZnGaON sample; (c) high resolution XPS spectrum of the N 1s peak in the ZnO–ZnGaON samples; (d) estimated Zn/Ga atomic ratio in the ZnO–ZnGaON sample from the XPS depth profile analysis. (Enlarged XPS images are shown in Fig. S2 in the ESI.†)

This journal is © The Royal Society of Chemistry 2014

Energy Environ. Sci., 2014, **7**, 1693–1699 | **1695**

techniques, XRD measurement is precise in the determination of small lattice mismatches, and thus, the difference in the ZnO and ZnO–ZnGaON samples can be observed. As shown in the XRD patterns in Fig. 3a, the synthesized ZnO and ZnO–ZnGaON nanowire electrodes are single crystalline in the wurtzite structure with the unique out-of-plane orientation of ZnO [0002]. Moreover, the (0001) diffraction peak of the ZnO–ZnGaON sample is asymmetric, and shifts to a higher 2θ angle compared to the symmetric ZnO (0001) diffraction peak. This result agrees with the reported XRD pattern of the ZnO:GaN powder that Ga and N incorporation decreases the lattice parameters of ZnO and thus increases the diffraction 2θ angle.[20] To further evidence this shift of the (0001) diffraction peak in the ZnO–ZnGaON nanowire sample, we fabricated ZnO and ZnO–ZnGaON samples made of short nanowires on thin films, so that the XRD diffraction peaks of the a-plane sapphire substrates can be clearly seen and used as a reference peak to compare the differences in (0001) diffraction peaks in the samples (see Fig. 3b). It is clearly observed that the (0001) diffraction peak of the ZnO–ZnGaON nanowire sample is composed of two diffraction peaks, one of them being shifted to a higher 2θ diffraction angle. Therefore, the single crystalline ZnO–ZnGaON nanowire-array-on-a-film samples are synthesized.

To elucidate the optoelectronic properties of the ZnO and ZnO–ZnGaON samples, ultraviolet-visible (UV-VIS) light diffuse reflectance and electrochemical impedance spectroscopy (EIS) analyses were conducted. Fig. 4a shows the UV-VIS absorption spectra of the ZnO and ZnO–ZnGaON nanowire samples. In the absorption spectrum of the ZnO sample, one sharp near-band-gap absorption edge at ~3.2 eV corresponding to the band gap
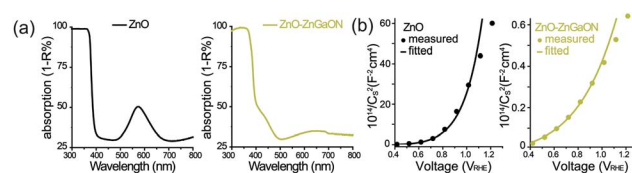

Fig. 4 Optoelectronic characterization of the ZnO and ZnO–ZnGaON nanowire-array-on-a-film samples: (a) UV-VIS diffuse reflectance curves of the samples; (b) EIS analyses of the samples taken at a frequency of 1 kHz under dark conditions with bias sweeping from 0.4 to 1.3 V_{RHE}.

value of ZnO is observed. In contrast, two absorption edges at ~3.0 eV and ~2.5 eV, with an intensity ratio of 2 : 1, were obtained for the ZnO–ZnGaON sample. The absorption edge at ~3.0 eV, red-shifted from the ~3.2 eV absorption edge, is likely attributed to absorption caused by N incorporation into ZnO. The absorption edge at ~2.5 eV is accounted for the band gap absorption of ZnGaON. It was reported that the presence of Zn 3d and N 2p electron orbitals in the valence band of ZnGaON results in a p–d repulsion effect, and thus the ZnGaON valence band maximum is shifted upward, leading to a reduced band gap rendering visible light absorption possible.[22] The observed absorption edge value of ~2.5 eV is also in agreement with the reported absorption edge of the ZnGaON.[20–22] Fig. 4b shows the EIS data of the fabricated ZnO and ZnO–ZnGaON nanowire samples. The ZnO and ZnO–ZnGaON samples consist of nanowire arrays so that each nanowire forms a quasi-cylindrical capacitance at its nanowire/electrolyte interface. Therefore, the capacitance per area (C_S) of the measured samples is mainly contributed by the quasi-cylindrical capacitances at the nanowire/electrolyte interfaces. A simple planar semiconductor/electrolyte model is not suitable to estimate the carrier density of the samples. Direct evidence to this point is that the shape of the measured EIS curves of $(1/C_S)^2$ versus voltage deviates from a linear behavior which is always obtained in the case of a planar semiconductor/electrolyte interface. Therefore considering the nanowire geometry effect, the Mora-Seró model[32] is used to fit the $(1/C_S)^2$ vs. voltage curve so that the carrier density of the ZnO and ZnO–ZnGaON nanowire samples can be estimated. The fitted carrier density of the ZnO sample is ~10^{17} cm^{-3}, which is consistent with the reported carrier density value of ZnO grown by vapor-phase deposition methods.[22] In comparison, the carrier density of the ZnO–ZnGaON sample is ~5×10^{18} cm^{-3}. The increase in carrier density is due to the incorporation of strong and highly soluble donor Ga in the ZnO nanostructures. This also suggests that N incorporation into the ZnO is well-controlled without causing ruinous defects or cracks in the ZnO–ZnGaON sample. As a result, the conductivity is improved in the ZnO–ZnGaON sample, leading to an enhanced PEC water splitting performance.

The PEC performance of the ZnO and ZnO–ZnGaON nanowire-array-on-a-film photoanodes was investigated using a three-electrode electrochemical configuration in a 0.5 M Na$_2$SO$_4$ solution buffered with NaOH at pH = 13 under standardized sunlight illumination (AM 1.5G, 100 mW cm^{-2}). An Ag/AgCl electrode in saturated KCl solution was used as a reference
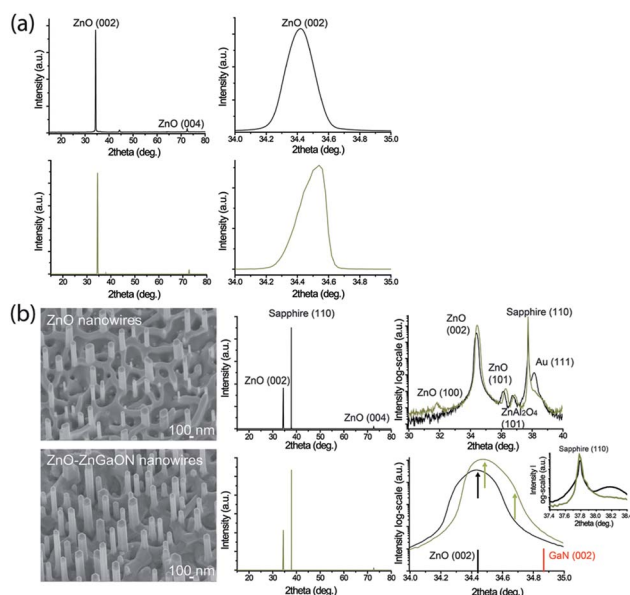

Fig. 3 XRD $\theta - 2\theta$ measurements of the synthesized ZnO and ZnO–ZnGaON nanowire-array-on-a-film photoanodes. (b) SEM images (left) and XRD $\theta - 2\theta$ measurements (right) of the ZnO and ZnO–ZnGaON short nanowire on thin film samples. (Enlarged XRD and SEM images are shown in Fig. S3 in the ESI.†)

1696 | *Energy Environ. Sci.*, 2014, **7**, 1693–1699

This journal is © The Royal Society of Chemistry 2014

electrode and a Pt coil was used as a counter electrode. The measured potentials *versus* Ag/AgCl were all converted to the reversible hydrogen electrode scale according to the Nernst equation,

$$V_{RHE} = V_{Ag/AgCl} + 0.059 \, pH + V^{\circ}_{Ag/AgCl},$$

$$V^{\circ}_{Ag/AgCl} = 0.199 \text{ V at 25 °C.}$$

Fig. 5a presents the current–potentiometry scan result of the ZnO and ZnO–ZnGaON photoanodes without loading of any co-catalyst with a sweeping bias from 0 to 1.45 V_{RHE} in light on–off cycles. Compared to the ZnO photoanode, the saturated photocurrent density value of the ZnO–ZnGaON photoanode reaches 1.75 mA cm^{-2} under sunlight illumination and it is larger than that of 1.25 mA cm^{-2} obtained with the ZnO photoanode under sunlight illumination. Using a different light source of 300 W xenon lamp, the saturated photocurrent density of the ZnO–ZnGaON photoanode is ~16 mA cm^{-2} and it is larger than that of ~10 mA cm^{-2} obtained with the ZnO photoanode (see Fig. S4 in the ESI†). Therefore, the increased photocurrent density with the ZnO–ZnGaON photoanode likely contributes to the increased light absorption in the ZnO–ZnGaON photoanode instead of the increased conductivity. The PEC performances of the synthesized ZnO, ZnO–ZnGa$_2$O$_4$ and ZnO–ZnGaON photoanodes are discussed in detail in the ESI.†

Fig. 5b presents the current–potentiometry light on–off scan results of the ZnO–ZnGaON photoanode. A clear photocurrent response of the ZnO–ZnGaON anode is observed with light on–off cycles. A low dark current density below 10^{-4} mA cm^{-2} was found during the light off cycles, which is a strong indication that light illumination is required for water oxidation to take place. Upon sunlight illumination, an anodic photocurrent appeared at a bias of ~0.3 V_{RHE}, rapidly increased with the bias from 0.3 to 0.8 V_{RHE}, and finally reached a plateau at ~1.7 mA cm^{-2} for an applied bias larger than 0.8 V_{RHE}.

The appearance of the anodic photocurrent at ~0.3 V_{RHE} indicates the onset potential of the ZnO–ZnGaON anode in the PEC current–potentiometry measurement. The slow increase in the photocurrent at the applied bias of ~0.3 V_{RHE} implies slow kinetics of water oxidation reaction when the applied bias is

close to the flatband potential of the ZnO–ZnGaON photoanode.[33] It appears that most of the photogenerated electrons and holes are recombined in the ZnO–ZnGaON photoanode for applied biases below 0.3 V_{RHE}, resulting in a relative low photocurrent density and low water splitting efficiency. When the bias is increased from 0.3 to 0.8 V_{RHE}, a rapid increase in the photocurrent density from 0 to 1.7 mA cm^{-2} is observed. The large increase in the photocurrent density is attributed to the drastic increase in the water oxidation reactions at the anode/electrolyte interfaces. It appears that an appreciable amount of photogenerated holes could transport across the photoanode/electrolyte interface and support water oxidation reactions with a sufficiently positive bias. Also, the electron depletion layer at the nanowire/electrolyte interface is widened with the increased applied bias, agreeing with the ZnO–ZnGaON EIS analysis results, so that the electron–hole recombination is suppressed and the increased water oxidation reaction rate is observed. When the applied bias is over 0.8 V_{RHE}, a large and saturated photocurrent density of ~1.7 mA cm^{-2} is obtained. Note that the plateau for the photocurrent density is evidence for a saturation behavior, which indicates an efficient transport of the photogenerated holes toward the photoanode/electrolyte interface in contrast to the non-saturated photocurrent density behavior for electron–hole recombination. This observed saturation behavior is an important characteristic indicating a high quality ZnO–ZnGaON photoanode.

The solar energy conversion efficiency (η) is calculated from the current–potentiometry data using the following equation:

$$\eta = J(1.23 - V_{RHE})/P_{sunlight},$$

where V_{RHE} is the applied voltage *versus* the reversible hydrogen electrode, J is the measured photocurrent density, and $P_{sunlight}$ is the incident light irradiance.

A maximum solar energy conversion efficiency of 0.75% (see Fig. 5b) is achieved with the ZnO–ZnGaON photoanode without the assistance of any co-catalysts. Compared to most of the oxide/oxynitride efficiencies reported in the literature, the high efficiency of 0.75% in this study is attributed to the formation of the conductive and visible-light-sensitive photoanode with the high-aspect-ratio nanostructure. Further improvements in the ZnO–ZnGaON photoanode efficiency could be anticipated by surface decoration with robust water oxidation co-catalysts to increase the water oxidation kinetics.

Finally, the PEC water splitting stability of the ZnO and ZnO–ZnGaON photoanodes was investigated by amperometric I–t (current–time) studies using the same Na$_2$SO$_4$ solution buffered with NaOH at pH = 13 in a three-electrode configuration at a fixed bias of 0.8 V_{RHE} (see Fig. 5). Both ZnO and ZnO–ZnGaON photoanodes show stable photocurrent in the amperometric study and have clear light on–off behaviour in the current–potentiometry scans before and after the amperometric study. However, SEM observations evidence that the density of the ZnO nanowires decreases with the increase of amperometric test time and, finally, all the ZnO nanowires were totally etched out resulting in the formation of a nanoporous film after 5.5 hours of amperometric test (see Fig. S5 in the ESI†). In clear
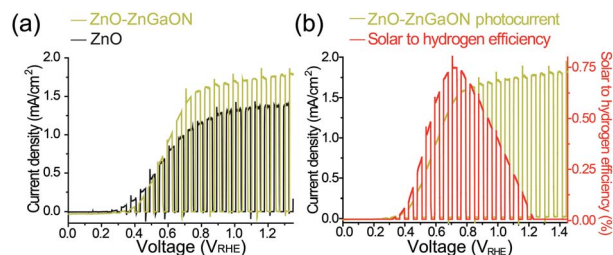

Fig. 5 PEC water oxidation performance: (a) photocurrent density of the ZnO (black) and ZnO–ZnGaON (yellow) photoanodes with applied voltage sweeping from 0 to 1.4 V_{RHE} in light on–off cycles; (b) photocurrent density of the ZnO–ZnGaON (yellow) photoanodes and their corresponding solar conversion efficiency (red) at different applied bias.
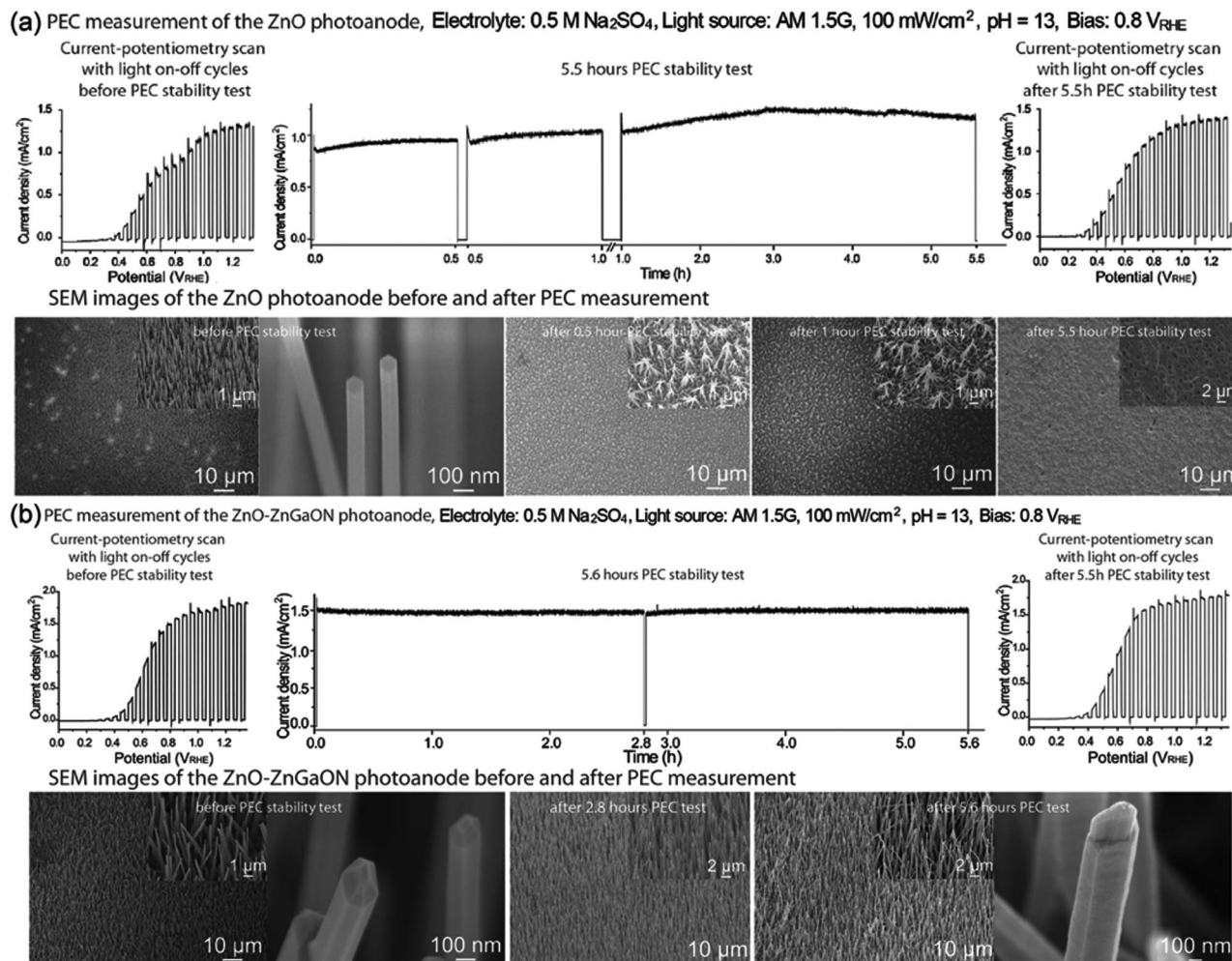
Fig. 6 PEC amperometric *I*−*t* (current−time) studies of the (a) ZnO and (b) ZnO−ZnGaON photoanodes. Top panels in (a) and (b) are light on−off current−potentiometry scans and amperometric *I*−*t* scans and bottom panels in (a) and (b) are photoanode SEM images after different amperometric scan times.

contrast, no noticeable degradation of the ZnO–ZnGaON nanowire structure is found after 5.6 hours of amperometric test from SEM observations. Therefore, the formation of Ga–O and Ga–N chemical bonds on the surface of ZnO nanowires stabilizes the material under PEC water oxidation conditions and good anti-photocorrosive ability of the ZnO–ZnGaON photoanode is inferred (Fig. 6).

In conclusion, we have demonstrated a stable and efficient sunlight water-splitting photoanode made of the ZnO–ZnGaON nanowire-array-on-a-film structure without using any co-catalyst. The significant PEC improvements of long-stability and high-efficiency are achieved owing to the conductive and high-crystalline oxynitride nanostructure with an anti-photocorrosive surface. As evidenced in the XPS, UV-VIS diffuse reflectance and EIS analyses, Ga and N are chemically incorporated into the ZnO to form ZnGaON on the surface of ZnO nanowires. Incorporation of N narrows the band gap and enables visible light absorption. Ga increases the conductivity for efficient charge transport and strengthens the chemical bonds against photocorrosion under water oxidation conditions. A photocurrent

density of ~1.7 mA cm^{-2} exhibiting a saturation behavior is obtained at an applied bias over 0.8 V_{RHE} and a solar energy conversion efficiency of 0.75% is achieved with the ZnO–ZnGaON photoanode under standard sunlight illumination. A very stable photocurrent density of ~1.5 mA cm^{-2} is obtained at the applied bias of 0.8 V_{RHE} with the ZnO–ZnGaON photoanode under continuous sunlight illumination over 5.6 hours. The present study demonstrates that the formation of ZnGaON on the surface of ZnO nanowires can efficiently improve chemical stability for photoelectrochemical water oxidation. Further, the conductive and high-aspect-ratio ZnO nanowire-array-on-a-film structure is a high-quality template that can be applied for the synthesis of other stable and powerful photocatalysts to contribute to efficient energy conversion applications.

Acknowledgements

References

1 S. W. Boettcher, E. L. Warren, M. C. Putnam, E. A. Santori, D. Turner-Evans, M. D. Kelzenberg, M. G. Walter, J. R. Mckone, B. S. Brunschwig, H. A. Atwater and N. S. Lewis, *J. Am. Chem. Soc.*, 2011, **133**, 1216–1219.

2 Y. Lin, G. Yuan, S. Sheehan, S. Zhou and D. Wang, *Energy Environ. Sci.*, 2011, **4**, 4862–4869.

3 X. Chen, L. Liu, P. Y. Yu and S. S. Mao, *Science*, 2011, **331**, 746–750.

4 K. Iwashina and A. Kudo, *J. Am. Chem. Soc.*, 2011, **133**, 13272–13275.

5 M. Liu, X. Qiu, M. Miyauchi and K. Hashimoto, *J. Am. Chem. Soc.*, 2013, **135**(27), 10064–10072.

6 H. Gao, C. Liu, H. E. Jeong and P. Yang, *ACS Nano*, 2012, **6**, 234–240.

7 T. Bak, J. Nowotny, M. Rekas and C. C. Sorrell, *Int. J. Hydrogen Energy*, 2002, **27**, 991–1022.

8 E. L. Warren, J. R. McKone, H. A. Atwater, H. B. Gray and N. S. Lewis, *Energy Environ. Sci.*, 2012, **5**, 9653–9661.

9 S. K. Karuturi, J. Luo, C. Cheng, L. Liu, L. T. Su, A. L. Y. Tok and H. J. Fan, *Adv. Mater.*, 2012, **24**, 4157–4162.

10 G. Wang, H. Wang, Y. Ling, Y. Tang, X. Yang, R. C. Fitzmorris, C. Wang, J. Z. Zhang and Y. Li, *Nano Lett.*, 2011, **11**, 3026–3033.

11 M. Xu, P. Da, H. Wu, D. Zhao and G. Zheng, *Nano Lett.*, 2012, **12**, 1503–1508.

12 M. Liu, N. D. L. Snapp and H. Park, *Chem. Sci.*, 2011, **2**, 80–87.

13 O. Khaselev and J. A. Turner, *Science*, 1998, **280**, 425–427.

14 C. Lin, Y. Lai, D. Mersch and E. Reisner, *Chem. Sci.*, 2012, **3**, 3482–3487.

15 J. Brillet, J. Yum, M. Cornuz, T. Hisatomi, R. Solarska, J. Augustynski, M. Grätzel and K. Sivula, *Nat. Photonics*, 2012, **6**, 824–828.

16 M. W. Kanan and D. G. Nocera, *Science*, 2008, **321**, 1072–1075.

17 Q. Yin, J. M. Tan, C. Besson, Y. V. Geletii, D. G. Musaev, A. E. Kuznetsov, Z. Luo, K. I. Hardcastle and C. L. Hill, *Science*, 2010, **328**, 342–345.

18 D. R. Gamelin, *Nat. Chem.*, 2012, **4**, 965–967.

19 Y. Li, T. Takata, D. Cha, K. Takanabe, T. Minegishi, J. Kubota and K. Domen, *Adv. Mater.*, 2013, **25**, 125–131.

20 K. Meada, T. Takata, M. Hara, N. Saito, Y. Inoue, H. Kobayashi and K. Domen, *J. Am. Chem. Soc.*, 2005, **127**, 8286–8287.

21 T. Ohno, L. Bai, T. Hisatomi, K. Maeda and K. Domen, *J. Am. Chem. Soc.*, 2012, **134**, 8254–8259.

22 K. Meada and K. Domen, *Chem. Mater.*, 2010, **22**, 612–623.

23 M. Mapa, K. S. Thushara, B. Saha, P. Chakraborty, C. M. Janet, R. P. Viswanath, N. Madhavan, K. V. G. K. Murty and C. S. Gopinath, *Chem. Mater.*, 2009, **21**, 2973–2979.

24 K. Lee, B. M. Tienes, M. B. Wilker, K. J. Schnitzenbaumer and G. Dukovic, *Nano Lett.*, 2012, **12**, 3268–3272.

25 M. Zhong, Y. Sato, M. Kurniawan, A. Apostoluk, B. Masenelli, E. Maeda, Y. Ikuhara and J.-J. Delaunay, *Nanotechnology*, 2012, **23**, 495602.

26 Binding energy peak of C 1s is detected in the ZnO XPS survey spectrum, implying the attachment of carbon impurity on the surface of the ZnO nanowires. It is suggested that the carbon impurity comes from the graphite precursor used in our first CVD process (see ref. 22). This C 1s peak is not detected in the ZnO–ZnGaON XPS survey spectrum, because the carbon impurity on the ZnO surface was burnt out in our second-step CVD process at a high temperature above 800 °C.

27 M. Zhong, Y. Li, Y. Yamada and J.-J. Delaunay, *Nanoscale*, 2012, **4**, 1509–1514.

28 X. Yang, A. Wolcott, G. Wang, A. Sobo, R. C. Fitzmorris, F. Qian, J. Z. Zhang and Y. Li, *Nano Lett.*, 2009, **9**, 2331–2336.

29 C. L. Perkins, S. Lee, X. Li, S. E. Asher and T. J. Coutts, *J. Appl. Phys.*, 2005, **97**, 034907.

30 K. Toyoura, H. Tsujimura, T. Goto, K. Hachiya, R. Hagiwara and Y. Ito, *Thin Solid Films*, 2005, **492**, 88–92.

31 K. Meada, K. Teramura, T. Takata, M. Hara, N. Saito, K. Toda, Y. Inoue, H. Kobayashi and K. Domen, *J. Phys. Chem. B*, 2005, **109**, 20504–20510.

32 I. Mora-Seró, F. Fabregat-Santiago, B. Denier and J. Bisquert, *Appl. Phys. Lett.*, 2006, **89**, 203117.

33 S. D. Tilley, M. Cornuz, K. Sivula and M. Grätzel, *Angew. Chem.*, 2010, **49**, 6405–6408.